

Learning Spatial Relationships between Samples of Image Shapes

Juan Castorena, Manish Bhattarai and Diane Oyen *

Abstract

Many applications including image based classification and retrieval of scientific and patent documents involve images in which brightness or color is not representative of content. In such cases, it seems intuitive to perform analysis on image shapes rather than on texture variations (i.e., pixel values). Here, we propose a method that combines sparsely sampling points from image shapes and learning the spatial relationships between the extracted samples that characterize them. A dynamic graph CNN producing a different graph at each layer is trained and used as the learning engine of node and edge features in a classification/retrieval task. Our set of experiments on multiple datasets demonstrate a variety of point sampling sparsities, training-set size, rigid body transformations and scaling; and show that the accuracy of our approach is less likely to degrade due to small training sets or transformations on the data.

1. Introduction

In the last decade image analysis underwent a revolution thanks to the advances in machine learning in particular those of deep learning (DL) [1]. Image classification, retrieval, detection, prediction, compression and general image analysis tasks saw performances that outperformed state of the art methods in applications including remote sensing, medical imaging, self-driving cars and general robotics. The driving engine of such advances are convolutional neural networks (CNN's) [2] that exploit the richness of textural information on images to learn shift-invariant features characterizing the image content. Some of the main properties of such architectures are the ability to learn the fundamental features across different scales, its computational efficiency due to the Fourier convolutional theorem, the reduced number of parameters required by CNN's in comparison to fully-connected layers and finally the flexibility to parallelize algorithms.

Unfortunately, many problem domains involve analysis of texture-less images. Examples of which include classification and retrieval of scientific or patent documents for which brightness or color is not representative of the content. For such cases, standard CNN's operating in the Euclidean domain can suffer significantly since convolutional filters are learned based on variations in texture. Figure 1 illustrates an example of the classification errors the traditional CNN from [2] can make with a simple gray scale inversion transformation. Such CNN model was learned with 99% accuracy on the raw MNIST dataset [2] and the example in Fig. 1 shows the classification results on an unseen raw 0 digit image in Fig. 1.a and on its corresponding inverted image in Fig. 1.b. The vector values in Fig. 1 represent the certainty of the classifier in each of the 10 digit cases. This, more or less illustrates that CNN's operating on the Euclidean domain of pixel values are not invariant to significant texture variations which causes classification performance degradation.

*J. Castorena, M. Bhattarai and D. Oyen are with the Los Alamos National Laboratory, Los Alamos, NM, 87545 USA
e-mail: {jcastorena, ceodsppectrum, doyen}@lanl.gov

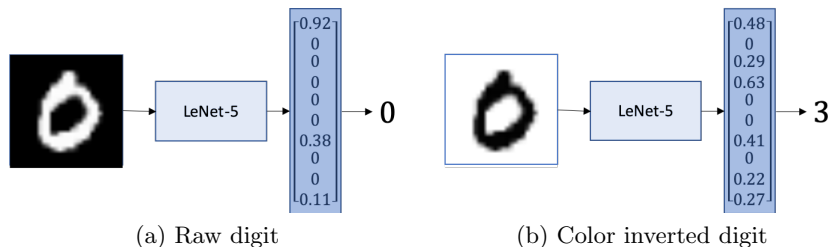


Figure 1: CNN miss-classification from color inversion.

Moreover, many analysis applications operate on images that consist of a variety of components whose spatial relationships and/or orientations between them is in some sense important. For such cases standard Euclidean domain CNN's have no capabilities but are rather merely dependent on the presence of such components. To illustrate this, we train a CNN on a binary classifier task with 100% accuracy. Representative examples of the two classes from the test dataset are shown in Figure 2a.b for which the CNN classifies correctly with high certainty. In contrast, Figure 2c.d show miss-classifications on the example of b when it underwent a shape transformation shifting the upper and lower components of the 8 digit, independently. This illustrates two points: 1) that CNN's do not care much about the spatial relationships between components but rather of their presence and 2) that CNN's are not invariant to rigid body transformations when those examples are not seen in training. Note that under rigid body transformation invariance Fig. 2d should have been classified to the same class as Fig. 2a.

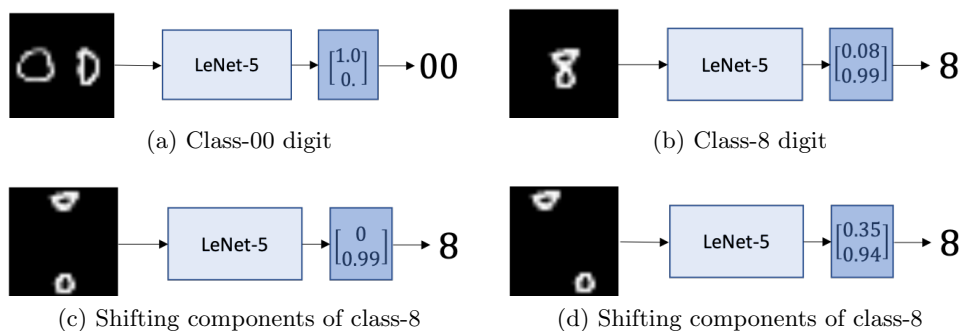


Figure 2: CNN miss-classification from shifting components.

Research in methods operating on image shapes rather than on texture have concentrated on fitting geometrical primitives including lines, circles, ellipses and curves to shapes by means of voting schemes. One example of which is the seminal Hough transform paper [3] and the more recent work by [4] for manifolds. However, fitting of geometrical primitives to shapes is a highly complex problem and computationally intensive specially in the case when the geometrical primitives dictionary is large with many probable rigid body transformations across scales. Not to mention that additional issues may exist when fitting due to the presence of shape deformations from noise and/or imperfect drawing.

Instead of directly analyzing shapes from their geometrical primitive components, another avenue focuses on the analysis of signals interacting with shapes, one instance of which is [5] analyzing the diffusion of signals on shapes. This, based on the idea that one could extract shape information by analyzing the signatures of signal-to-shape interactions. Recent work exploiting such a paradigm combined it with non-Euclidean neural net learning mechanisms to characterize geometric shapes. Such efforts dubbed

as geometric DL [6] have produced state of the art results in shape correspondence/matching, shape classification and retrieval, dimensionality reduction, and network analysis applications. For example, the work by [7] focused on generalizing the Fourier convolution theorem by performing analysis in the spectral domain of 3D shapes including graphs and manifolds. One drawback though is that the learned features generalize poorly to other shapes since the convolution like operator is not translation invariant [6]. The work of [8, 9] instead approximated convolution operators in the spatial domain. Such filters apply convolution-like geodesic operations to local patches around points similar to the tangential space equivalent in Riemannian manifolds. The methods have better generalization capabilities, however, the learned features exploit local information only whereby additional global information could be of potential benefit.

Our contribution in this research is a method combining the extraction of sparse point clouds from image shapes and learning local and global spatial relationships between the points that characterize shapes. We contend that learning graph node and edge relationships can aid in such characterization and propose the use of the dynamic graph CNN (DGCNN) of [10]. Such an architecture includes modules that learn both local and global features diffusing non-locally across layers for improved inference. Given this, our paper presents the proposed approach in Section 2. Section 3 presents experimental results to study classification/retrieval performance against scaling, rotations, translations, training dataset size and point cloud sparsity on a variety of datasets, and finally Section 4 concludes our findings.

2. Approach

The basis of the method we propose consists on the extraction of shapes from images, point sampling from the shape and finally learning node and edge interconnection features that characterize shape point samples. A summary of the system is shown in Figure 3.



Figure 3: Image shape analysis system.

2.1. Point clouds from image shapes

Shapes are first extracted from images by segmenting shape from background through the well known adaptive thresholding method of Otsu [11]. Note that the use of a shape segmentation method is a necessity only in cases when images are non-binary. Such an extraction and analysis on the non-Euclidean spatial composition of a shape instead of the Euclidean analysis on image pixel values will enable the learning engine to be invariant against image texture or color; a property of crucial importance to many applications.

Following, a representative sparse point-cloud of the shape is extracted by clustering the pixel locations conforming the segmented shape. The algorithm we use here for such clustering is the mini-batch k -means [12] which is orders of magnitude more computationally efficient than standard k -means with only small penalties in performance. The efficiency of such method is obtained by processing data iteratively in batches of randomly picked points with centroids computed through stochastic gradient descent (SGD). Each of the estimated S centroids denoted here by $\mathbf{x}_i^{(0)} \in \mathbb{R}^2$ for $i \in \{1, \dots, S\}$ contains the corresponding (x, y) location of the estimates. Comforming all of the k -means centroids results in a point cloud $\mathbf{X}^{(0)} = \{\mathbf{x}_1^{(0)}, \dots, \mathbf{x}_S^{(0)}\}$ of sparsely sampled representative points of the shape. Note that, throughout this paper the superscript (0) denotes an input.

2.2. Learning shapes through graphs

The sampled points $\mathbf{X}^{(0)}$ of the shape are used as input to a deep neural net that learns features characterizing the meaningful spatial relationships between the points. Here, the sampled points and their spatial relationships are represented as nodes and edges of a graph, respectively. The learning engine of such graphs is a dynamic graph CNN (DGCNN) [10] architecture dynamically operating and learning graphs across its layers. Here, each layer l produces graphs $\mathcal{G}_m^{(l)} = (\mathcal{V}^{(l)}, \mathcal{E}_m^{(l)})$ indexed by $m \in \{1, \dots, M^{(l)}\}$ by dynamically associating k nearest learned feature neighbors (f- k NN's) according to node distances in the feature space. An instance of the DGCNN architecture we use is shown in Figure 4. Such

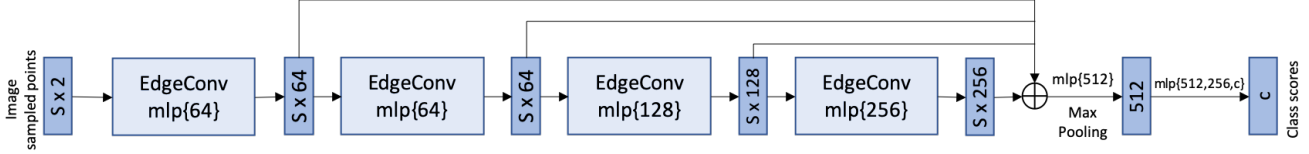


Figure 4: Dynamic Graph CNN Architecture.

an architecture consists of a sequence of $M^{(l)}$ -dim edgeConv layers consisting each of node and edge connection features $\mathbf{x}_i^{(l)} \in \mathbb{R}^{M^{(l)}}$ for $i \in \mathcal{V}^{(l)}$ and $\mathbf{e}_{ij}^{(l)} \in \mathbb{R}^{M^{(l)}}$ for $(i, j) \in \mathcal{E}_m^{(l)}$, respectively. Node features $x_{im}^{(l)}$ are computed element-wise as

$$x_{im}^{(l)} = \max_{j:(i,j) \in \mathcal{E}_m^{(l)}} e_{ijm}^{(l)} \quad (1)$$

where the maximum is computed over the f- k NN's at the node i and edge features computed element-wise as

$$e_{ijm}^{(l)} = \text{ReLU}(\boldsymbol{\theta}_m^{(l)} \cdot (\mathbf{x}_j^{(l-1)} - \mathbf{x}_i^{(l-1)}) + \boldsymbol{\phi}_m^{(l)} \cdot \mathbf{x}_i^{(l-1)}) \quad (2)$$

with $\boldsymbol{\theta}_m^{(l)}, \boldsymbol{\phi}_m^{(l)} \in \mathbb{R}^{M^{(l)}}$ being parameters of the learned convolution filters. Note that the first inner product in Eq (2) captures local information whereas the second inner product captures global information. Fig. 5 illustrates the mechanism by which the edgeConv layer generates features in a node. First it computes the f- k NNs j_{i_1}, \dots, j_{i_5} centered at node i using Euclidean distances between features. Then, computes functions e'_{ijm} in Eq. (2) through the learned filters only for the f- k NNs and then applies (1). Implementations of these operators can be framed as a shared multi-layer perceptron (mlp).

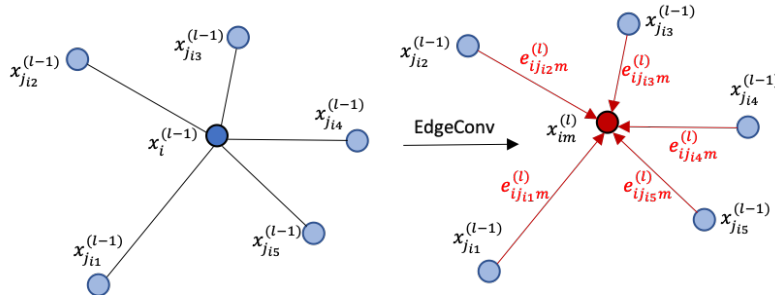


Figure 5: EdgeConv at a node.

3. Experiments

Evaluation of the proposed approach is tested against the task of classification of the MNIST benchmark [2], the fashion-MNIST [13] and the CLEF-IP dataset of patent images in [14]. The datasets are partitioned into balanced-class training and testing subsets.

3.1. Point cloud extraction

We generate a point-cloud for each image shape in the aforementioned datasets following Section 2.1. Figure 6 illustrates a few representative point cloud examples where the first row shows the MNIST digit images and the second row represents the corresponding extracted point clouds. The point-clouds are each of size 10×2 (i.e., $S = 10$) for which case the mini-batched k -means algorithm runs near real-time and thus does not represent a significant computational bottleneck. Here, we also observe

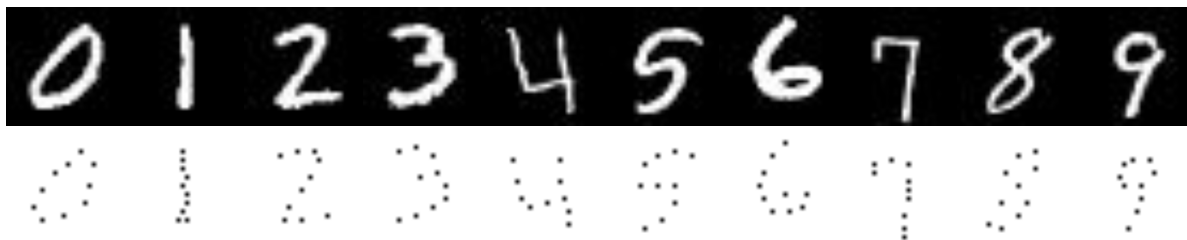


Figure 6: Sampling points from MNIST digit images. Row 1: MNIST images, Row 2: Sampled points.

that the proposed sampling mechanism captures the underlying structure of the MNIST shapes even when $S = 10$. For illustration purposes we also include in Figure 7 an example that shows the effect of increasing sparsity. Note that at the sparsest point cloud it is visually difficult to identify the digit and some ambiguity exists as to whether it is a 2, 3 or an 8. Fortunately, with sparsity of at least $S = 10$ the digit can be identified. Such effect is consistent with at least a vast number of examples manually inspected from the MNIST.

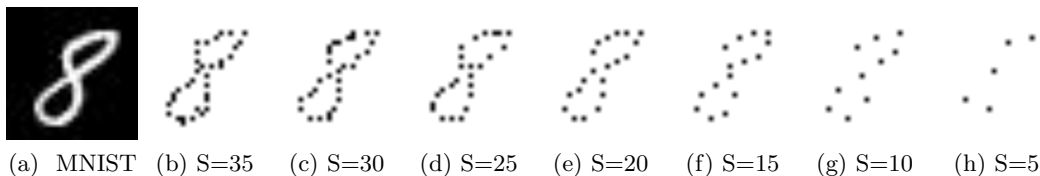


Figure 7: MNIST digit point cloud as a function of sparsity

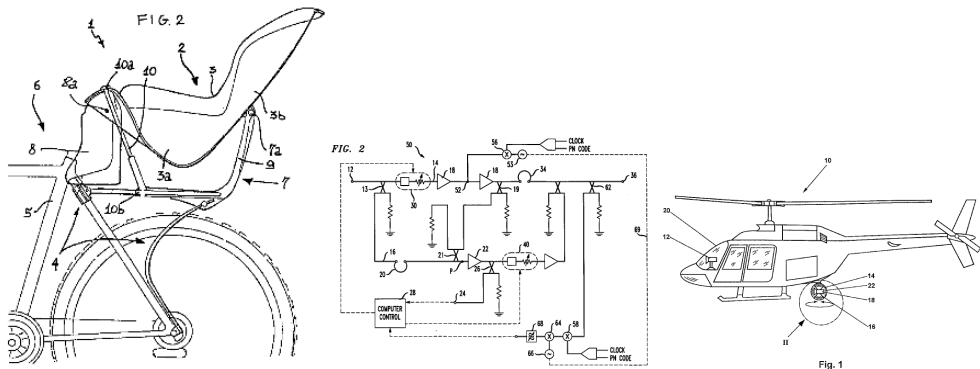
To make fashion-MNIST more like patent images, we process images to produce their corresponding spatial gradient magnitudes and extract point-clouds from this. The gradient magnitude is computed from the anisotropic first order forward difference components in the horizontal and vertical directions. Figure 8 includes representative examples (one per class) where the first and second row represents the gradient magnitude and the extracted point-clouds with sparsity $S = 50$, respectively. Note that again in this case, the point-cloud sampled from the images visually preserves the shapes therein, however, these have point-clouds of less sparsity in comparison to MNIST.

For illustrative purposes we include representative examples of the sampled shapes extracted from CLEF-IP's [14] images extracted from patent documents. The first column in Fig. 9 are the raw images while the second column is the result of sparsely sampling the image shape with $S = 1000$. Note that the

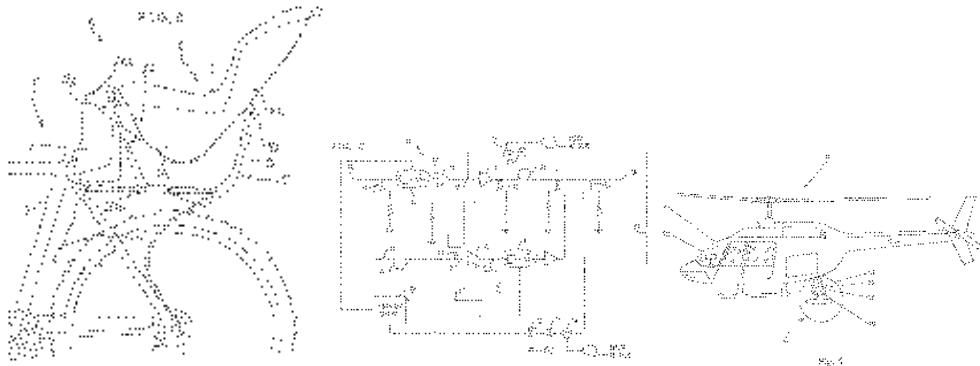


Figure 8: Sampling points from fashion-MNIST. Row 1: images, Row 2: Sampled points.

sampling mechanism we employ visually preserves the shapes in all three cases as long as the point-cloud is relatively dense.



(a) Bike seat image 2254×1854 (b) Circuit image 920×1248 (c) Helicopter image 964×1440



(d) Sampled image shape (e) Sampled image shape (f) Sampled image shape

Figure 9: Sparse sampling of CLEF-IP image shapes.

3.2. Classification

Following the architecture model of [10] we use four EdgeConv layers as shown in Figure 4 of which the first three are fully-connected producing, respectively, features of size (64, 64, 128, 256). Max/sum pooling is used, unless otherwise specified the number of f-kNN is set to 5, dropout with keep probability of 0.5 and all layers include LeakyReLU and batch normalization.

For training, we use stochastic gradient descent (SGD) with self-adaptive learning rate. The rule to

self-adapt is based on the warm restart method of [15] with an initial value of 0.1. Batch size is set to 32, momentum for batch normalization is set to 0.9 and $\#epochs = 100$. We tested performance with a variety of number of parameters and the ones selected are the ones that yielded the best results.

Shapes are extracted from the image datasets by first transforming them into binary images through segmentation with Otsu’s adaptive thresholding method [11]. After the shape-background segmentation, each shape is sampled following the method description in Section 2.1. A point cloud of size $S \times 2$ is obtained for each 28×28 image that is subsequently centered and normalized to be within the unit ℓ_2 -norm ball.

The first set of experiments is intended to obtain MNIST classification performance against the sparsity of the point cloud extracted from the image shapes. For this, partitions of 42K and 28K images were utilized to train and test, correspondingly. Figure 10 illustrates classification performance as a function of point cloud sparsity. Our results validate the intuition that classification accuracies suffer when using point-cloud inputs of higher sparsity. This becomes more significant when due to sparsity the shape can no longer be identifiable from other sampled shapes as observed in Figure 7 for $S = 5$.

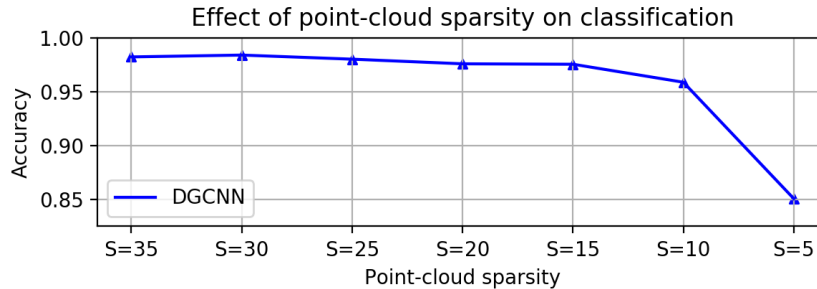


Figure 10: Classification versus point cloud sparsity.

A comparison of MNIST classification performance against other methods as training dataset size is varied was also conducted with results included in Fig. 11. The methods we compared against are the LeNet-5 [2] with full 28×28 image inputs and with those obtained by using PointNet [16] in place of the DGCNN architecture. We observe that the DGCNN model consistently outperforms PointNet at all training dataset sizes. This indicates that the addition of modules to learn global features in the DGCNN improves shape characterizations over PointNet learning only local shape features. When comparing against LeNet-5, our findings show that the proposed method learns features that generalize better to training dataset size reductions in comparison to LeNet-5.

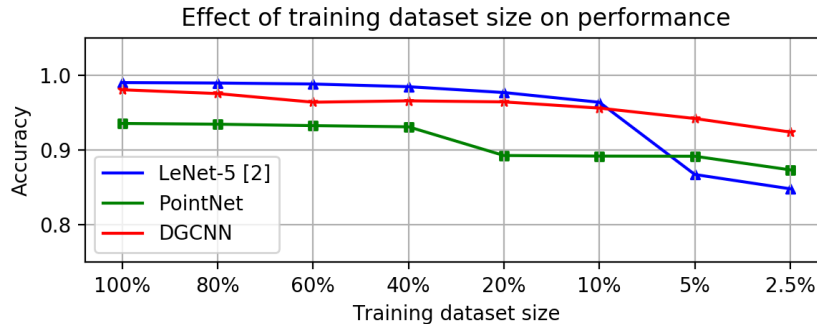


Figure 11: Classification versus training dataset size.

Additional evaluations on classification were performed now against the effect of rigid body transformations and scaling in the 2D image plane of the MNIST images on performance. For this purpose, we first train and test by transforming MNIST with random uniformly sampled $\pm 90^\circ$ rotations, ± 9 pixel translations in both horizontal and vertical directions and by (0.2,1) scaling each transformation applied independently. Second, we train and test performance against the three transformations applied altogether to the MNIST dataset. In such case, rotations, translations and scaling are randomly sampled from a uniform distribution with limits $\pm 90^\circ$, ± 9 pixels and 0.3 for rotation, translation and scaling, respectively. Table 1 summarizes the comparison results of performance against transformations of the MNIST dataset. These results show that our proposed framework performs better than standard CNN’s

Table 1: Classification against MNIST transformations.

Method	scaled MNIST	rot MNIST	translate MNIST	scaled, rot, translate MNIST
LeNet5 [2]	0.961	0.981	0.976	0.874
Proposed	0.985	0.933	0.995	0.935

operating in the Euclidean domain. The centering and ℓ_2 normalization of point clouds from extracted shapes makes our method fully invariant to scaling and translation transformations while invariance to rotations in the image plane is learned by the neural net. In general, we can say that analysis of shapes extracted from images with the proposed method is in some sense invariant to rigid body transformations in the 2D plane across scales. However, this is not necessarily true for general 3D-2D projections and more studies need to be conducted.

Classification performance for the fashion-MNIST is also tested with results included in Table 2. Here, we include performance comparisons against the methods also referenced therein. With such benchmark we use a point shape sampling sparsity of $S = 50$ and $k = 25$ as the f- k NN. Classification performance in the human case was obtained through the labeling from a non-fashion expert in a randomized dataset sample of size 1000. We note that the proposed method achieves better performance compared to classification by a non-fashion expert human. In addition, we also present results of the LeNet-5 [2] trained and tested on the raw fashion-MNIST whose performance outperforms that of ours. However, and for illustrative purposes we verify how invariant is this against color/gray scale transformations. This was done here with the raw image trained model and validated on the test dataset with image brightness inverted and the classification result we found on LeNet-5 is significantly reduced to 0.098 whereas our proposed method achieves same classification performance as in the non-inverted case. Thus, this confirms that our proposed method is invariant to brightness transformations as long as the shape can be effectively extracted.

Table 2: Classification of fashion-MNIST [13].

Method	LeNet-5 [2]	Human Performance	Proposed
	0.888	0.835	0.849

The final experiment on classification tests the proposed method against the CLEF-IP [14] patent image dataset. This dataset was built as a classification challenge including image categorization into one of

the 9 classes: drawing, flowchart, graph, symbol, math, table, program, chem, geneseq. A representative example of the images for each of these classes is shown in Figure 12. This dataset contains approximately 38K unbalanced-class images partitioned into the training and testing subsets. Each image was sampled and used as input to a DGCNN to learn the spatial relationships characterizing the shape classes. The sparsity of sampling was set in this case to $S = 1000$ and the f - k NN was set to 25. Intuition behind the usage of such sparsity is that in general the CLEF-IP contains much more complex shapes in comparison to both MNIST and fashion-MNIST and thus requires denser samplings. To learn the spatial relationships between the shape samples, the hyperparameters of the DGCNN were set to be the same as those described at the beginning of this section. The results we obtained for classification on the CLEF-IP dataset was of 0.877.

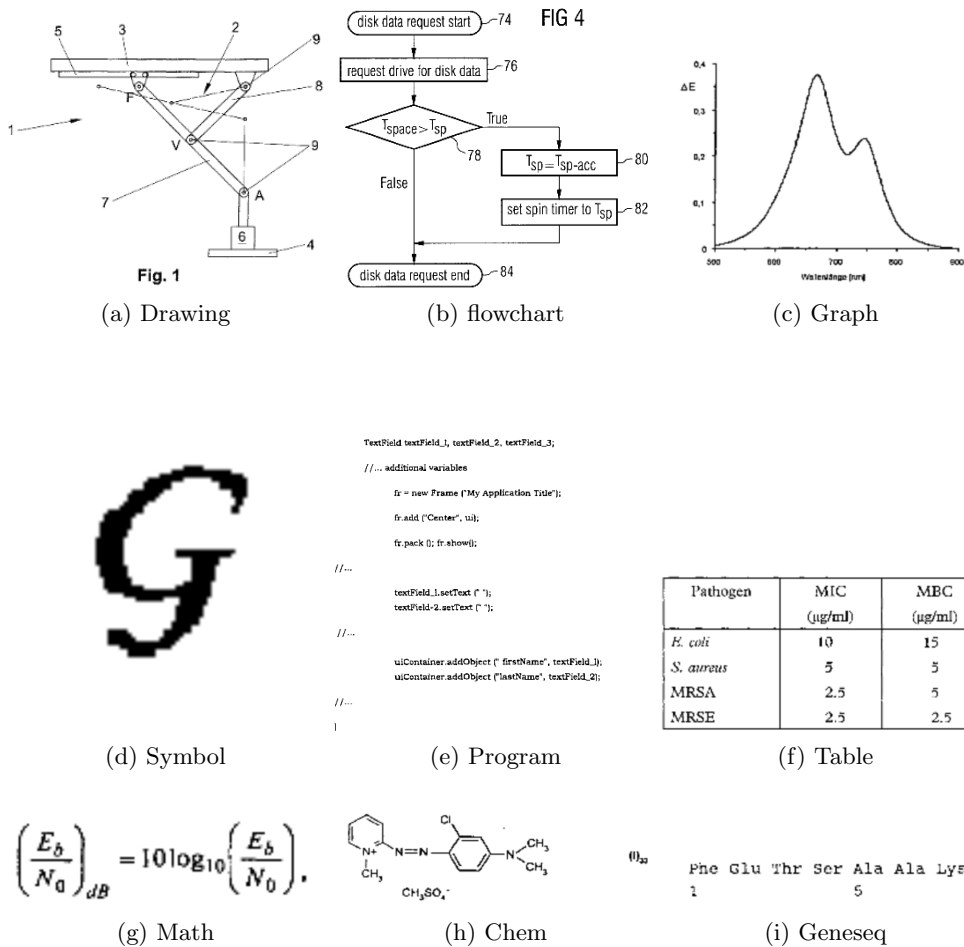


Figure 12: Examples of the CLEF-IP 9-class images.

3.3. Retrieval

In addition to the classification task we also compare the performance of the proposed approach against the standard structural similarity Index (SSIM) method [17] in a retrieval task. We tested against the MNIST, fashion-MNIST and CLEF-IP datasets described in the previous subsection and show that the proposed framework performs significantly better than the SSIM approach. To measure performance, we

use the mean average precision (MAP) overall retrievals computed as:

$$\text{MAP} = \frac{\sum_{q=1}^Q \text{Ave}(P(q))}{Q} \tag{3}$$

where Q is the number of queries and $\text{Ave}(P(q))$ is the precision average of score for each query q . Here, $\text{Ave}(P(q))$ is obtained by computing the average number of items correctly retrieved in a k nearest neighborhood.

In the case of the proposed method, we re-use the concatenated local and global features learned in the classification task after the fourth EdgeConv layer in Figure 4. For illustrative purposes we show how the learned features naturally cluster for the CLEF-IP dataset by using the t-Distributed Stochastic Neighbor Embedding(t-SNE) [18] projection. Note in Figure 13 that features are nicely packed which seem as promising to be used to effectively retrieve similar shapes. Standard SSIM computes the structural pair-



Figure 13: TSNE projection of the features extracted for CLEF-IP test dataset at the embedding layer of DGCNN.

wise similarity between all the image combinations in the test dataset partition and yields the set of k -images with the highest similarity measure given a query. With that, we summarize the MPA scores in both Figure 14 and in Table 3 for quantitative clarity. Here, we note that DGCNN outperforms SSIM in most cases, except on the MNIST dataset where there is a huge structural uniformity in similarity within class samples without significant view-point variations.

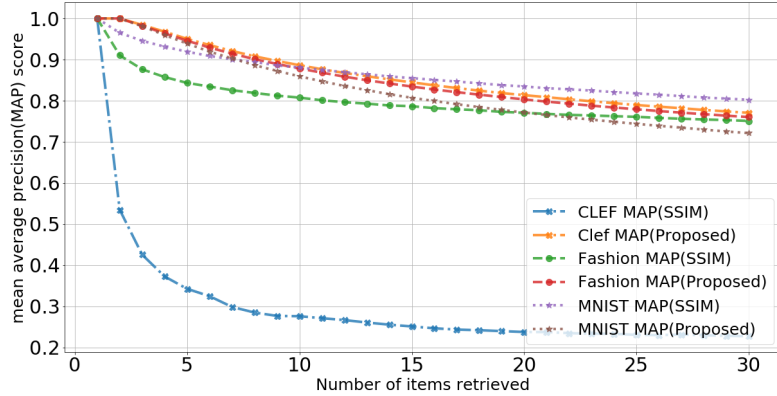


Figure 14: Mean average precision analysis for different datasets using SSIM vs proposed approach.

Table 3: Retrieval Performances.

Dataset	MAP @10 retrievals	MAP @20 retrievals	MAP @30 retrievals
MNIST	0.88(SSIM)	0.83(SSIM)	0.80(SSIM)
	0.86(DGCNN)	0.77(DGCNN)	0.72(DGCNN)
fashion-MNIST	0.807(SSIM)	0.770(SSIM)	0.750(SSIM)
	0.878(DGCNN)	0.803(DGCNN)	0.760(DGCNN)
CLEF-IP	0.276(SSIM)	0.238(SSIM)	0.227(SSIM)
	0.886(DGCNN)	0.814(DGCNN)	0.771(DGCNN)

4. Conclusion

In this work, we proposed a method for shape analysis based on a graph neural net that learns features defined both on sampled shape points and interconnections between them. Our experiments on classification/retrieval tasks of multiple datasets show that the proposed method performs competitively with state of the art methods in their own domain. In future work, we envision designing a graph learning net that exploits hierarchical point-cloud multi-sparsity level features from which we expect an improved performance in more complex shape cases. In addition, we will explore in detail ways to achieve invariance to shape perspective on performance.

References

- [1] Yann LeCun, Y Bengio, and Geoffrey Hinton, “Deep learning,” *Nature*, vol. 521, pp. 436–44, 05 2015.
- [2] Y. Lecun, L. Bottou, Y. Bengio, and P. Haffner, “Gradient-based learning applied to document recognition,” *Proceedings of the IEEE*, vol. 86, no. 11, pp. 2278–2324, Nov 1998.
- [3] D.H. Ballard, “Generalizing the hough transform to detect arbitrary shapes,” *Pattern Recognition*, vol. 13, no. 2, pp. 111 – 122, 1981.

- [4] Shay Deutsch and Grard Medioni, “Learning the geometric structure of manifolds with singularities using the tensor voting graph,” *J. Math. Imaging Vis.*, vol. 57, no. 3, pp. 402–422, Mar. 2017.
- [5] Ronald R. Coifman and Stphane Lafon, “Diffusion maps,” *Applied and Computational Harmonic Analysis*, vol. 21, no. 1, pp. 5 – 30, 2006, Special Issue: Diffusion Maps and Wavelets.
- [6] M. M. Bronstein, J. Bruna, Y. LeCun, A. Szlam, and P. Vandergheynst, “Geometric deep learning: Going beyond euclidean data,” *IEEE Signal Processing Magazine*, vol. 34, no. 4, pp. 18–42, July 2017.
- [7] Michaël Defferrard, Xavier Bresson, and Pierre Vandergheynst, “Convolutional neural networks on graphs with fast localized spectral filtering,” in *Proceedings of the 30th International Conference on Neural Information Processing Systems*, USA, 2016, NIPS’16, pp. 3844–3852, Curran Associates Inc.
- [8] J. Masci, D. Boscaini, M. M. Bronstein, and P. Vandergheynst, “Geodesic convolutional neural networks on riemannian manifolds,” in *2015 IEEE International Conference on Computer Vision Workshop (ICCVW)*, Dec 2015, pp. 832–840.
- [9] Federico Monti, Davide Boscaini, Jonathan Masci, Emanuele Rodol, Jan Svoboda, and Michael Bronstein, “Geometric deep learning on graphs and manifolds using mixture model cnns,” 07 2017, pp. 5425–5434.
- [10] Yue Wang, Yongbin Sun, Ziwei Liu, Sanjay E. Sarma, Michael M. Bronstein, and Justin M. Solomon, “Dynamic graph cnn for learning on point clouds,” *ACM Trans. Graph.*, vol. 38, no. 5, pp. 146:1–146:12, Oct. 2019.
- [11] N. Otsu, “A threshold selection method from gray-level histograms,” *IEEE Transactions on Systems, Man, and Cybernetics*, vol. 9, no. 1, pp. 62–66, Jan 1979.
- [12] D. Sculley, “Web-scale k-means clustering,” in *Proceedings of the 19th International Conference on World Wide Web*, New York, NY, USA, 2010, WWW 10, p. 11771178, Association for Computing Machinery.
- [13] Han Xiao, Kashif Rasul, and Roland Vollgraf, “Fashion-mnist: a novel image dataset for benchmarking machine learning algorithms,” 2017.
- [14] Florina Piroi, Mihai Lupu, Allan Hanbury, and Veronika Zenz, “Clef-ip 2011: Retrieval in the intellectual property domain,” in *CLEF*, 2011.
- [15] Ilya Loshchilov and Frank Hutter, “SGDR: stochastic gradient descent with restarts,” *CoRR*, vol. abs/1608.03983, 2016.
- [16] R. Q. Charles, H. Su, M. Kaichun, and L. J. Guibas, “Pointnet: Deep learning on point sets for 3d classification and segmentation,” in *2017 IEEE Conference on Computer Vision and Pattern Recognition (CVPR)*, July 2017, pp. 77–85.
- [17] Alain Hore and Djemel Ziou, “Image quality metrics: Psnr vs. ssim,” in *2010 20th International Conference on Pattern Recognition*. IEEE, 2010, pp. 2366–2369.
- [18] Laurens van der Maaten and Geoffrey Hinton, “Visualizing data using t-sne,” *Journal of machine learning research*, vol. 9, no. Nov, pp. 2579–2605, 2008.